ON THE INFLUENCE OF MICROSTRUCTURAL FEATURES OF LINEAR FRICTION WELDING AND ELECTRON BEAM ADDITIVE MANUFACTURING TI-6AL-4V ON TENSILE AND FATIGUE MECHANICAL PROPERTIES

Michael Mendoza (ISU)
Faculty: Peter Collins (ISU)
Industrial Mentor: Honeywell

35.1 Project Overview and Industrial Relevance

This research provides a study of Linear Friction Welding (LFW) and Electron Beam Additive Manufacturing (EBAM) of the alloy Ti-6Al-4V. Currently these technologies are suitable for many aerospace applications and, in particular for integrated blisks (i.e. aeroengine compressor discs with blades). However, more studies to understand the individual microstructure influence on mechanical properties are required. In this work, dogbone shape specimens were extracted from LFW-Ti-6AL-4V to individually assess the tensile mechanical properties of the Welded Zone (WZ), Thermo-mechanically affected Zone (TMAZ) and the Parent material zone (PM) across the weld line. Beam shape specimens were also extracted from EBAM-Ti-6Al-4V to evaluate the individual microstructure influence on fatigue mechanical properties by a four-point bending test. Finally, COMSOL Multiphysics software was used to predict shape and dimensions of cantilever specimens from EBAM-Ti-6Al-4V to again assess the individual microstructure influence on fatigue mechanical properties, but to a very high cycle's regime (10^9 Cycles). For this last section, a commercial ultrasonic welding machine will be adapted to perform the fatigue tests.

The study of Ti-6Al-4V under different manufacturing processes is attracting more interest from industry because of cost reduction and potential improvements in mechanical properties. The main advantage of LFW resides in the fact that for aircraft structural components oversized ingots are machined to get the final component, so a large amount of material is wasted. LFW allows the use of not oversized ingots for welding them together to form the component with less use of initial material.

35.2 Literature Review

The study of Ti-6Al-4V under different manufacturing processes is attracting more interest from industry because of cost reduction and potential improvements in mechanical properties. Each manufacturing process (e.g. LFW, EBAM, LENS, Casting, etc.) has its own particularities in terms of thermal or thermomechanical histories that affect local microstructures. However, we will focus on LFW that offers unique thermomechanical conditions and EBAM that provides bigger microstructural features than other AM processes which makes the analysis easier. Linear Friction Welding LFW is a solid-state joining process of two workpieces under compressive forces [35-1] (Fig. 1a). During the process, one workpiece is stationary while the other one is in motion, this friction generates heat that plasticize the contact zone and a final forging pressure is applied to consolidate the joint [35-2]. The current and major use of LFW is for joining of aeroengine compressor discs with blades to form blisks [35-3, 35-4, 35-5, 35-6] (Fig. 1b). However, there is more recent interest for aircraft structural components made of Ti-6Al-4V [35-6]. The main advantage of LFW resides in the fact that for aircraft structural components oversized ingots are machined to get the final component, so a large amount of material is wasted. Smaller workpieces can be joined with LFW to produce a component, so less material is required as an initial step [35-6]. Vairis and Frost [35-7, 35-8] describe the process into four distinct phases. At phase I, the two workpieces are placed into contact under certain pressure. The contact area is augmented with reduction of asperities and heat generation due to solid friction. In phase II, the heat generation is enough to increase the area of contact to a 100% and expulsion of viscous material from the interface (i.e. initial flash formation). In the specific case of Ti-6Al-4V, it is when the interface reaches the β-transus temperature [35-9]. Phase III is the equilibrium phase, here the flash formation is more visible and the axial shortening is present at a constant rate [35-6]. Phase IV is known as deceleration and forging phase where in less than 0.1 s the two workpieces are brought to rest and a final forging pressure is applied to finish the joint. LFW-Ti-6Al-4V can produces three different zones, parent or base material (PM) with a bi-modal microstructure (i.e. primary α_p grains surrounded by a lamellar microstructure of α laths
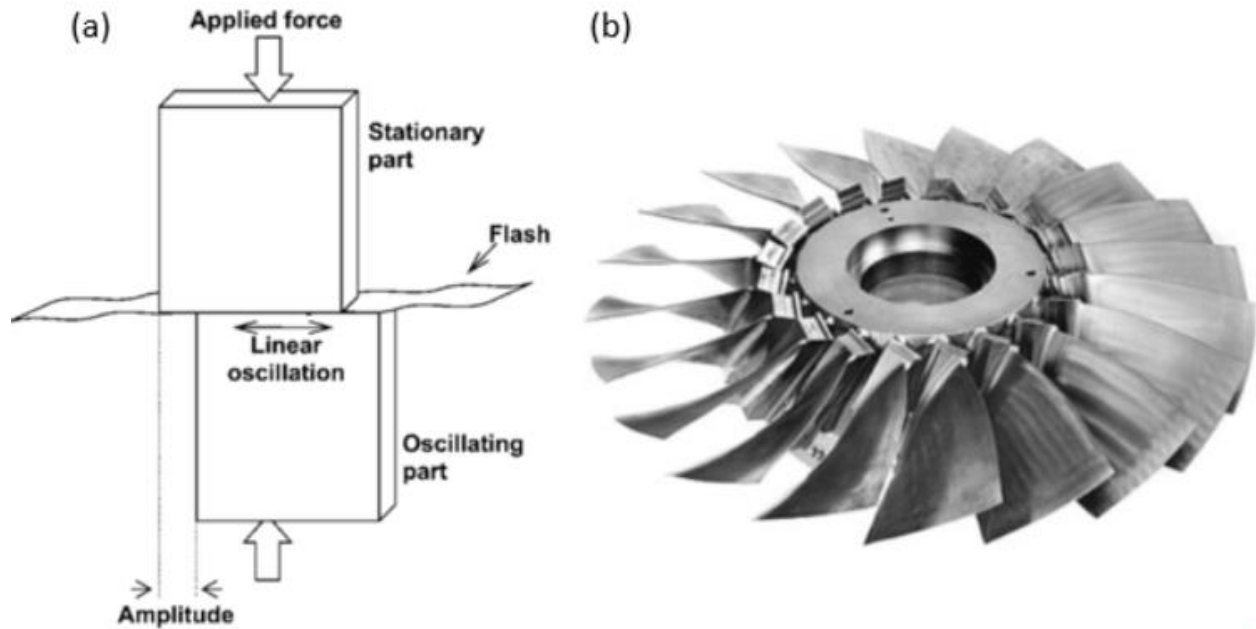
Figure 1.(a) Diagram of Linear Friction Welding process, (b) Integrated blisk (disc and blades) [35-3].

in a β matrix), thermo-mechanically affected zone (TMAZ) with a distorted bi-modal microstructure and a weld zone (WZ) with a refined martensitic α' (needle-like) or a widmanstatten microstructure depending on the cooling rate (Fig. 2).
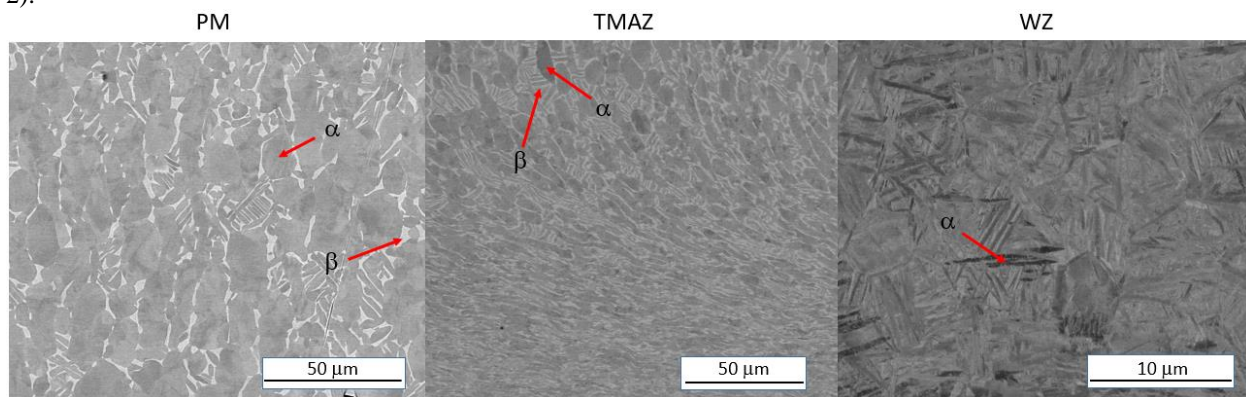
Fig. 2 Microstructure change across a LFW joint.

As mentioned, this research focus into the Ti-6Al-4V alloy and some mechanical properties according to the microstructure as a consequence of the manufacturing process. The conventional approach to evaluate tensile mechanical properties for LFW of Ti-6Al-4V is by consideration of processing parameters as the frequency of oscillation, amplitude, frictional pressure and axial shortening [35-1, 35-6, 35-10, 35-11, 35-12]. However, our approach will be just to evaluate specific tensile properties of given LFW-Ti-6Al-4V microstructures at certain constant processing parameters. To date most of the results for tensile test show failure at the parent material zone (PM) if not interface contaminants are present [35-1, 35-6, 35-10, 35-11, 35-12]. However, Wanjara and Jahazi [35-1] also showed that failure can also occur on the TMAZ due to a low power input that reduce the cooling rate after oscillatory motion, making the alpha laths bigger which in turn makes the TMAZ weaker than PM [35-6]. Our approach is to evaluate the specific tensile properties of the three zones of LFW-Ti-6Al-4V by forcing the tensile samples to fail at the respective zone. Characterization techniques as SEM, EBSD, TEM and PED will help us to determine the reasons of those differences in tensile properties.

Additive manufacturing process (AM), also known as 3D printing is a rapid solidification process that

involves several factors affecting the final microstructure. By definition AM is a process where a local heat source (e.g. laser, electron beam, plasma) melts a source of material (e.g. incoming powder flow, wire, powder bed) on a substrate of similar characteristics of the material [35-13]. The relative motion between the heat source and the substrate allows the melted material deposition to occur layer by layer, always under a computer aid control from a CAD file [35-13] (Fig. 3). This particular way to produce parts offers several advantages as near net-shape components with very low final machining required, complex parts are easy to make with the right CAD file, less waste of material as compared with subtractive manufacturing technologies and new possibilities in terms of microstructure control.
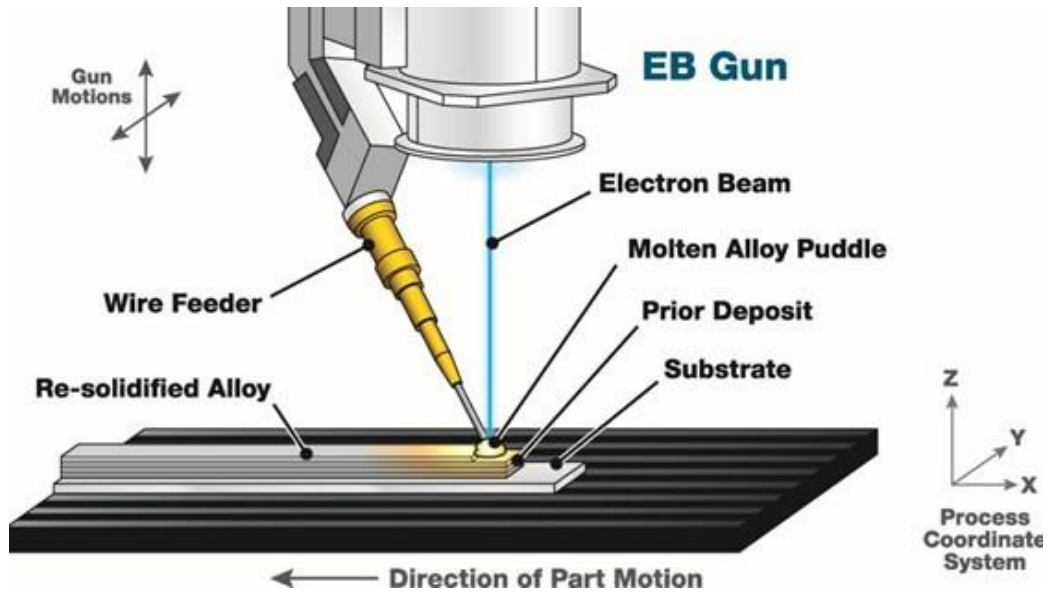
Fig. 3 Schematic EBAM® process [35-14].

In this study, we will focus into the Electron Beam Additive manufacturing technique EBAM® that uses an electron beam as heat source, Ti-6Al-4V wire as feedstock and a vacuum chamber to protect the alloy to react with oxygen. In Fig. 4 characteristic features of EBAM-Ti-6Al-4V are observed in the z-y cross-section being x the direction of deposition (out of paper). Two distinct zones can be recognize on this picture, zone A comprises vertically elongated prior β grains with very little variation in α lath thickness due to the uniform and strong epitaxial growth from bottom to top [35-15]. On the other hand, Zone B has a pronounced variation in α lath thickness and a more scattered orientation due to the competing growth from the side wall of the molten pool [35-15]. Several tensile tests were already reported on those microstructures to assess their influence on tensile mechanical properties [35-15]. Therefore, the interest of this research is in mechanical properties from a fatigue test on those two type of microstructures. Four-point bending test is selected as a convenient method for fatigue studies due to several reasons (Fig. 5). It typically works with rectangular beams that produce a uniform maximum stress on the surface, depending of the distance between inner rollers [35-16]. Easy sample mounting and dismounting as no special gripping is required. It is also suitable to evaluate specific microstructures from small samples, T. Zhai et al. [35-16] reported specific sample and device dimensions to perform the four-point bending test. The optimum testing geometry to achieve a uniform stress distribution consistent with the calculated value of beam theory, requires a load span/specimen thickness ratio (t/h) between 1.2 and 1.5. It also requires a support span/load span ratio (L/t) between 4 and 5 [35-16].
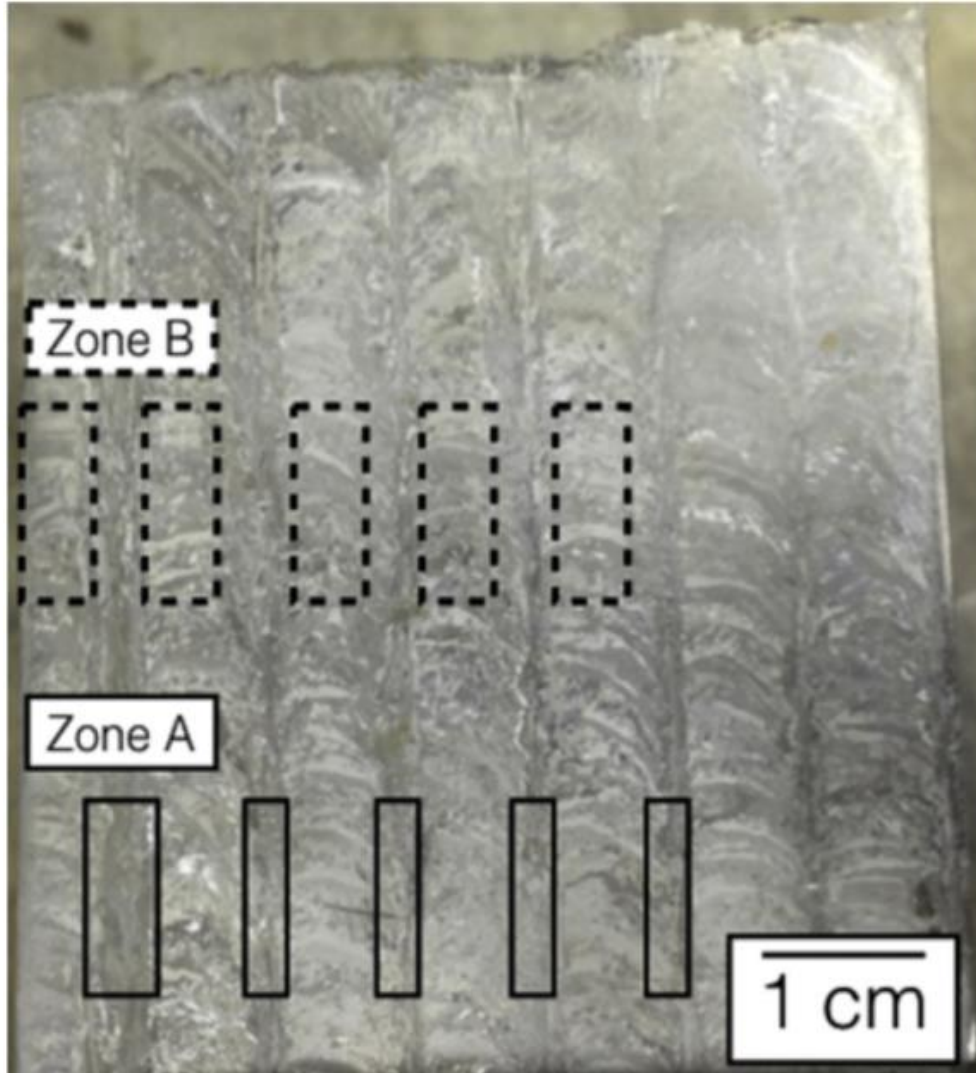
Fig. 4 Z-Y Cross-section of an ELI Ti-6Al-4V build [35-15].
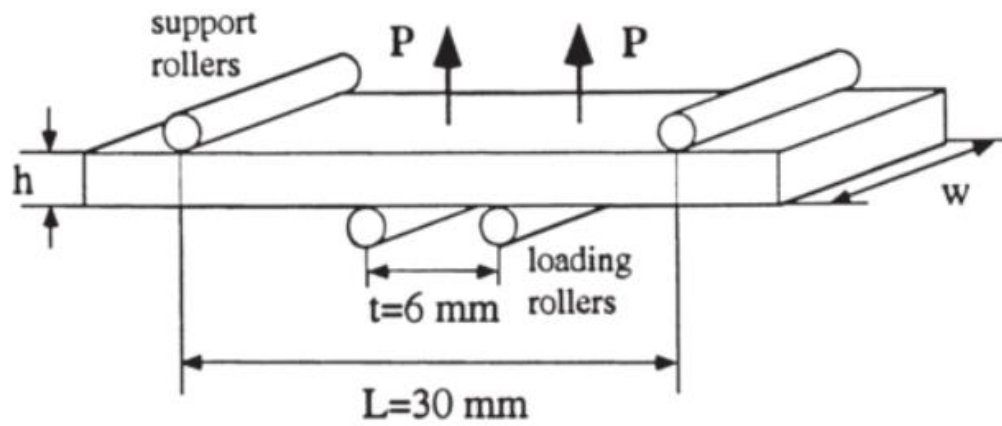
Fig. 5 Four-point bend specimen geometry and the loading states [35-16]

Conventional fatigue approach provides useful information of mechanical properties. However, several applications of Ti-alloys (e.g. Ti-6Al-4V) are required to safe operation over long periods of time, extending 10^9 cycles [35-17]. Conventional fatigue tests as electromagnetic shakers or servo-hydraulic systems can achieve 10^9 cycles in weeks, so a single S-N curve would last months [35-18]. This approach is impractical to understand the material behavior in this regime. Therefore, ultrasonic fatigue testing offers an alternative where 10^9 cycles can be reached in less than a day. An ultrasonic fatigue system contains a generator, transducers (piezoelectric elements that generate the mechanical movement), booster, acoustic horn (typically acting as amplifier) and specimen (Fig. 6). Each part of the system has to satisfy the resonance condition [35-19]. This design is made in a way where the specimen has specific dimensions to offer a mode shape with maximum amplitude deformation on the specimen and not on any other part of the system [35-19, 35-20, 35-21]. Usually 20 KHz ± 500 Hz is the Eigenfrequency used to perform fatigue tests, a more detailed ultrasonic fatigue testing description can be found in [35-18, 35-19, 35-20, 35-22, 35-23]. Our approach here is again to evaluate a selective microstructure of an EBAM-Ti-6Al-4V process as for the conventional fatigue case (10^7 cycles), but in the regime of very high cycles (10^9). For this purpose, we will use an ultrasonic welding machine manufactured by Branson Ultrasonics with certain modifications to perform the fatigue test. The pre-selection of booster, horn, specimen shape and dimensions will be based on simulations of the process by COMSOL Multiphysics. A more detailed description of the general steps for the simulation can be found in [35-24].

In this study, we have three general objectives. First, we will assess tensile mechanical properties of the individual LFW zones as WZ, TMAZ and PM. Second, we will evaluate conventional fatigue mechanical properties of two zones (microstructures) of an EBAM-Ti-6Al-4V process. Finally, we will extend the analysis of the fatigue mechanical properties of the EBAM-Ti-6Al-4V process under the very high cycle regime. Additionally, we will adapt an ultrasonic welding machine into an ultrasonic fatigue machine.
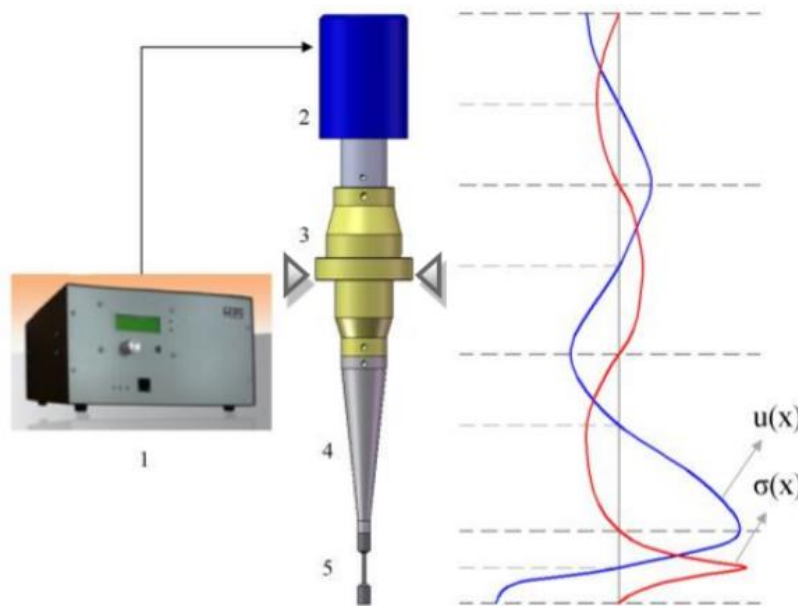
Fig. 6 Ultrasonic fatigue testing machine. 1-generator, 2- transducer, 3-booster, 4-horn, 5-specimen. u(x) displacement, σ(x) stress [35-24]

35.3   Tensile test and Dislocation Density

More dogbone shape samples were extracted via EDM (Electron Discharge Machining) according to the availability of LFW-Ti-6AL-4V material to improve the statistics of the three zones of the process (Fig. 7). A ZwickLine Z2.5TN with screw grips type 8253 was used again for the tensile test of the three LFW zones and the TestXpert II software registered the respective Stress/Strain data and curves (Fig. 8).

35. 5
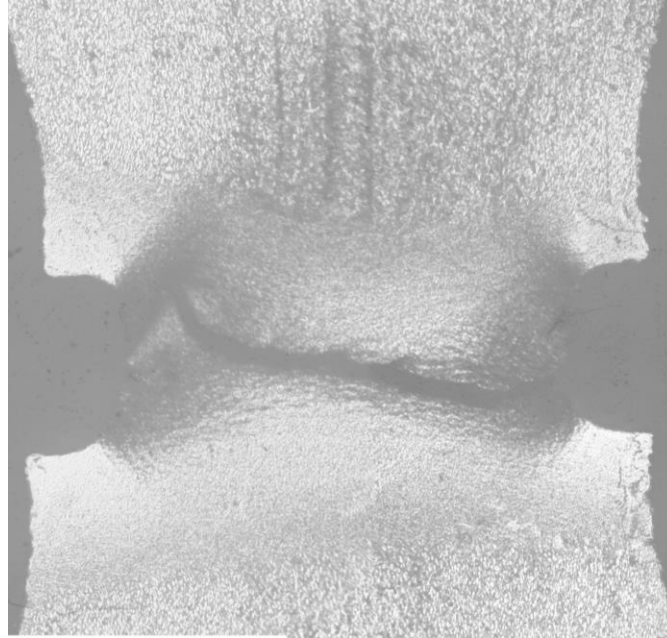
Fig. 7 WZ Tensile test specimens after test.
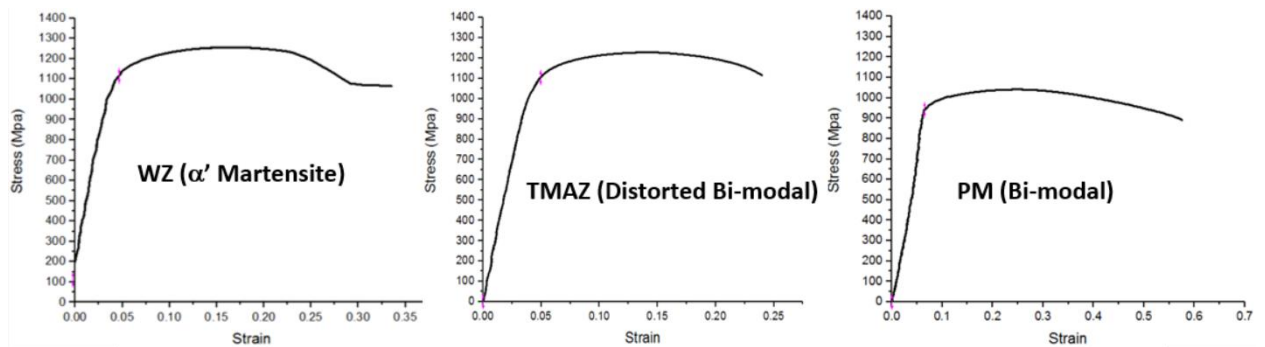
Fig. 8 Stress/ Strain curves for the three LFW-Ti-6Al-4V zones.

From this additional data, we can see that the yield strength is ~16% for the TMAZ and ~20% for the WZ greater than the PM zone. We know from similar tensile tests on LENS-Ti-6Al-4V that the yield stress is between 1 and 10% greater than the PM zone due to the martensitic microstructure. This difference suggests that another hardening mechanism is taking place.

Table. 1 Tensile properties of LFW-Ti-6AL-4V zones.

	$Y_{0.2\%}$ (Mpa)	U_{TS} (Mpa)	R_S (Mpa)	%El	Y_{HV} (Mpa)
WZ	1175	1259	1106	24.7	1324
TMAZ	1141	1245	1068	31.0	1196
PM	976	1040	886	56.4	1098

35. 6

In order to understand if strain hardening is taking place, PED-TEM analysis has been performed on the LFW zones to evaluate the dislocation density (Fig. 9). The Euler orientation information from PED is the input file for a MATLAB developed code [35-25] to calculate the dislocation density.
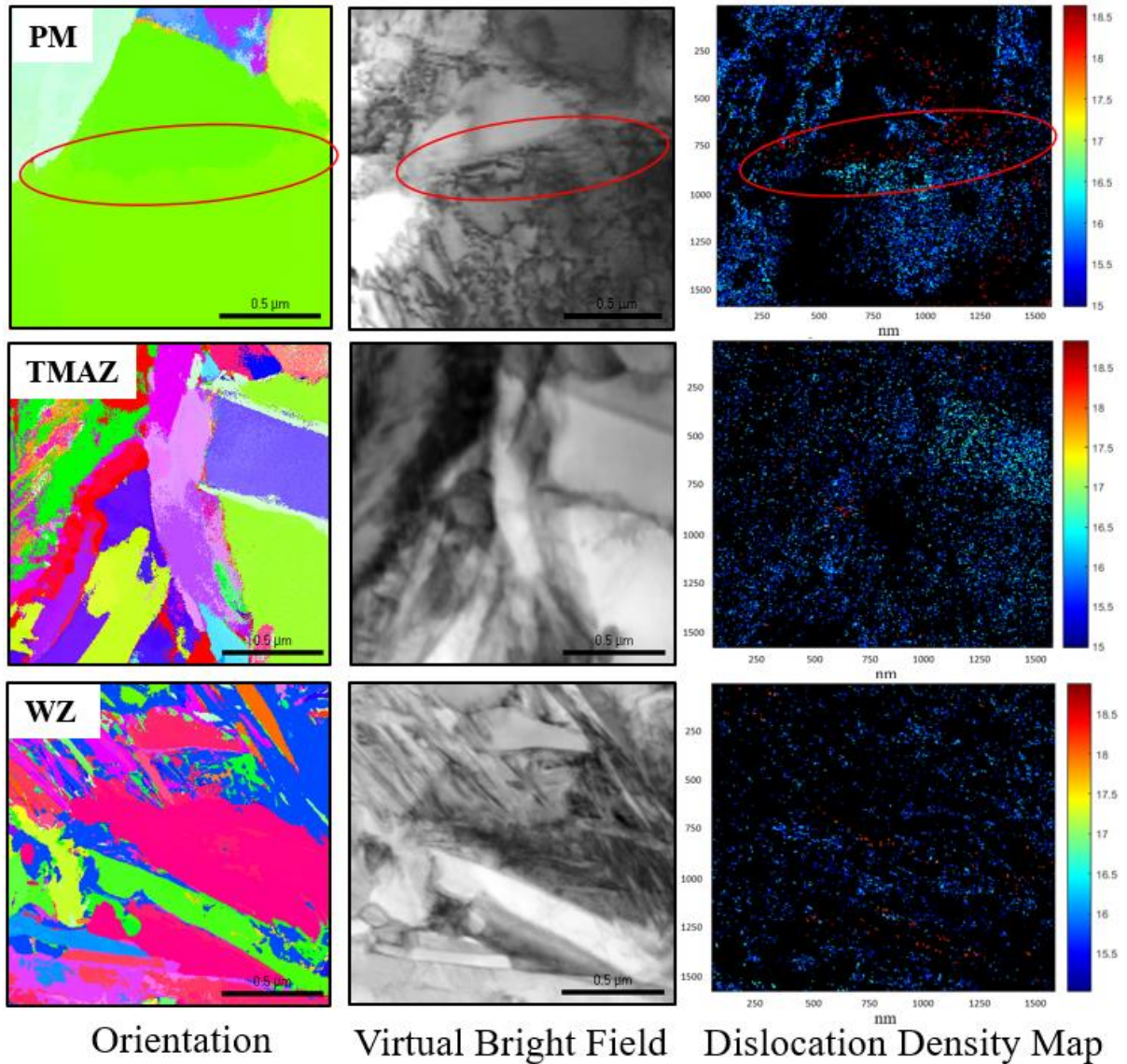
Figure 9 TEM-PED orientation and dislocation density calculation results

Figure 9 shows the orientation maps, virtual bright field obtained by the TEM-PED system and the dislocation density maps with average values from the MATLAB algorithm. The first observation is the unexpected higher value of average dislocation density for PM of $10^{17.0814}$ m^{-2} over $10^{16.5405}$ m^{-2} for TMAZ and 10^{169142} m^{-2} for WZ. However, some considerations have to be analyzed to properly interpret these results.

In linear friction welding process the PM region does not undergo any plastic deformation. This means that there is not any generation of new dislocations as compared with the TMAZ and WZ where plastic deformation does occur. A more detailed analysis of the bright field image of the PM and TMAZ reveals the presence of bending contours. These contours are localized, permanent bends in the specimen as a consequence of specimen preparation. They are regularly present in ductile thin foils and produce a lattice curvature (i.e. disorientation) that can lead to an

35. 7

overestimated dislocation density calculation. Figure 10 shows a better visualization of bending contours on PM. These results suggest that the values of dislocation density are not representing the pre-existence of GNDs.
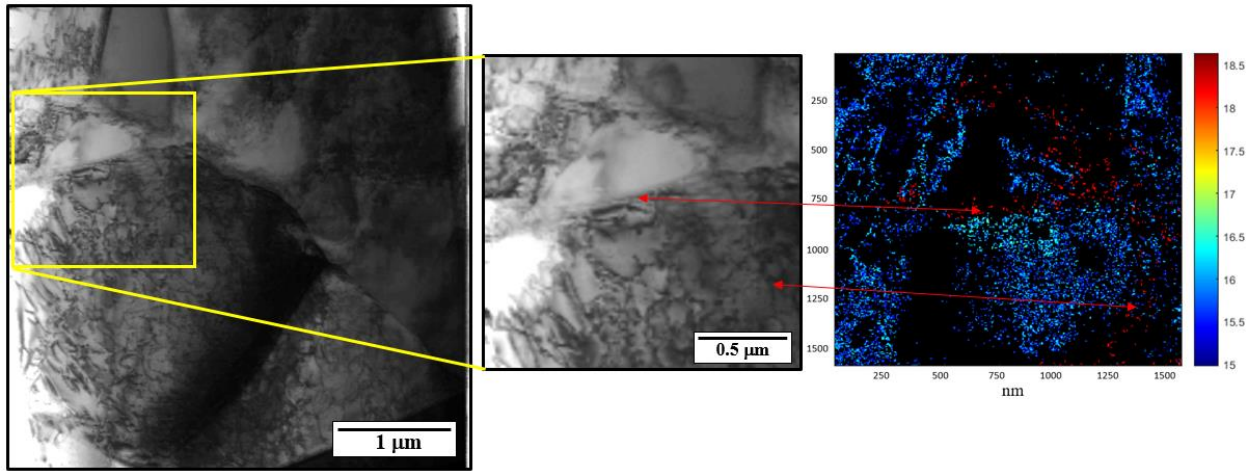
Figure 10 Bending contours in parent material region of LFW

Despite a quantitative representation of the average dislocation density was not possible through TEM-PED and calculation, other indicators show the trend of deformation's degree for the three LFW regions in the order of PM < TMAZ < WZ. The unindexed fraction on EBSD shows that trend and HKL channel 5 software can plot kernel average misorientation maps using the EBSD orientation information of each zone. Kernel average misorientation maps (KAM) show local misorientation associated to plastic deformation by averaging crystal orientation differences between a host pixel and its adjacent pixels. Figure 11 shows the three KAM maps for the three LFW regions. The scale color (blue to red) represents the degree of misorientation associated to plastic deformation from a 1st order neighbor (3 x 3 pixel) with a threshold angle of 5°. The trend is again clear on the same direction of unindexed fraction of EBSD data (PM < TMAZ < WZ). Possibly a quantitative description of this trend can be achieved by a bulk dislocation density measurement via X-Ray diffraction with the challenge of small size availability of the LFW regions, specially the TMAZ with a width of just ~200 μm.

In conclusion, the tensile test results show that WZ is about 20% greater than PM and TMAZ is about 13% greater than PM. Even when evidence of dislocation accumulation as a consequence of deformation was not possible via TEM-PED and calculations, the qualitative description given by the unindexing fraction of EBSD and the KAM maps suggest the action of strain hardening. The strain hardening inherent to the LFW process together with the martensitic microstructure constitute the explanation for the tensile test results. The PED approach to measure the dislocation density offers the high spatial resolution required to capture those dislocations generated by highly deformed or UFG (ultrafine grained) materials. However, this approach works under the assumption that bend contours are unlikely in highly deformed high-strength materials and among the LFW zones just the WZ may qualify. Therefore, it is proposed that in the future a bulk dislocation density calculation should be performed via X-ray diffraction or another alternative method.

Center Proprietary – Terms of CANFSA Membership Agreement Apply
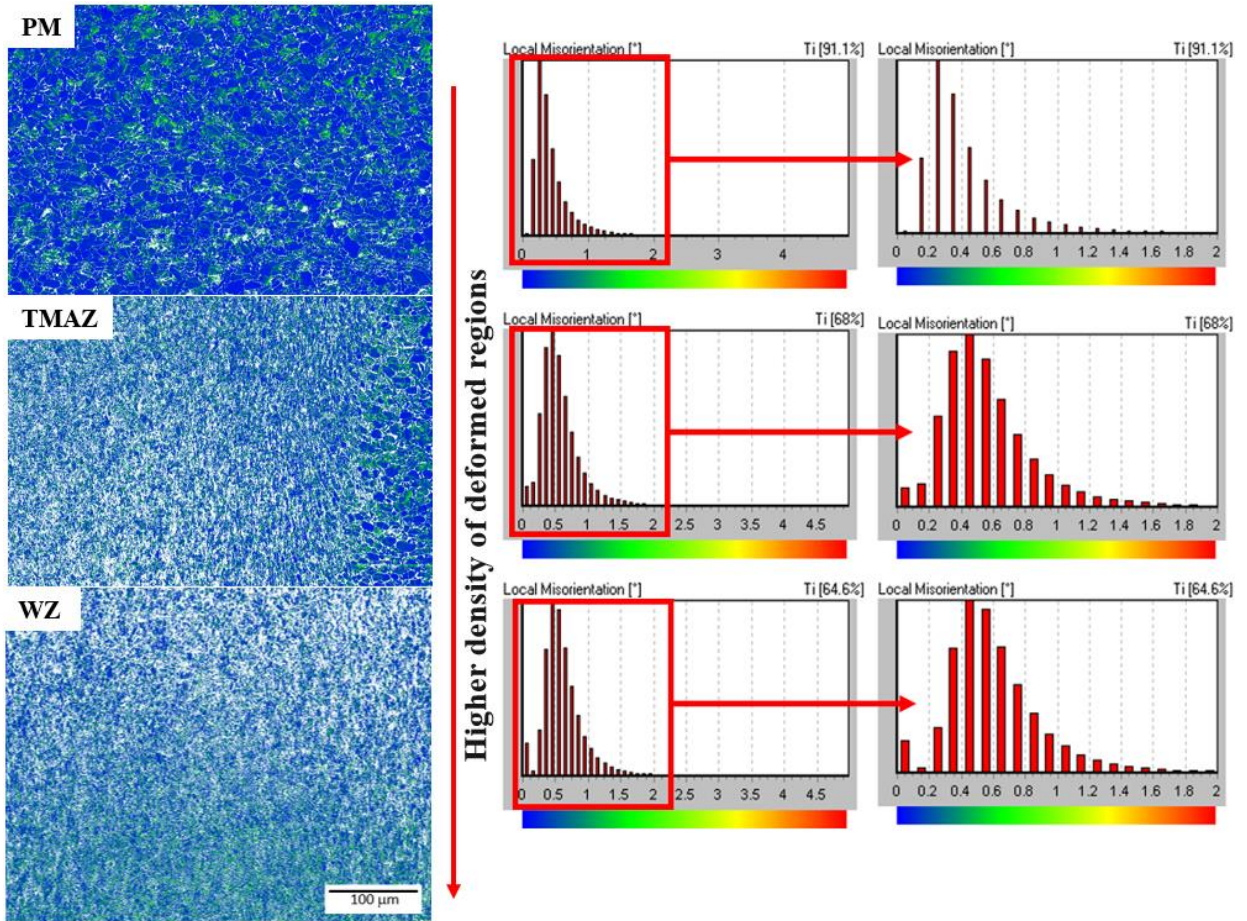
Figure 11 KAM maps of the three linear friction welding zones.

35.4   Conventional Fatigue Testing of EBAM®-Ti-6Al-4V

The four-point bending fatigue test was conducted by Westmoreland Mechanical Testing & Research, Inc. at room temperature on a servo-hydraulic machine employing a sinusoidal waveform. Figure 12 shows the captured features for specimens tested to evaluate the selected microstructures A and B. In figure 13, the stress life data curves reported by Westmoreland, Inc. shows that microstructure A (blue) has a better fatigue performance than B (red). The analysis to explain how the microstructure affects that behavior can be divided into two perspectives, crack initiation and crack propagation.
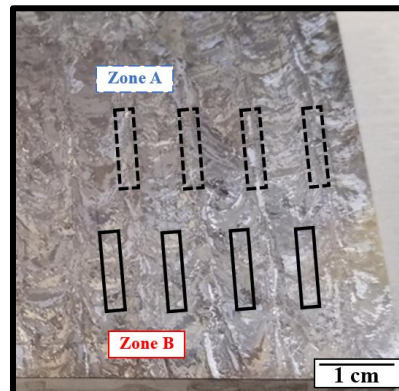
Figure 12 Microstructures A and B from EBAM-Ti-6Al-4V.

35. 9
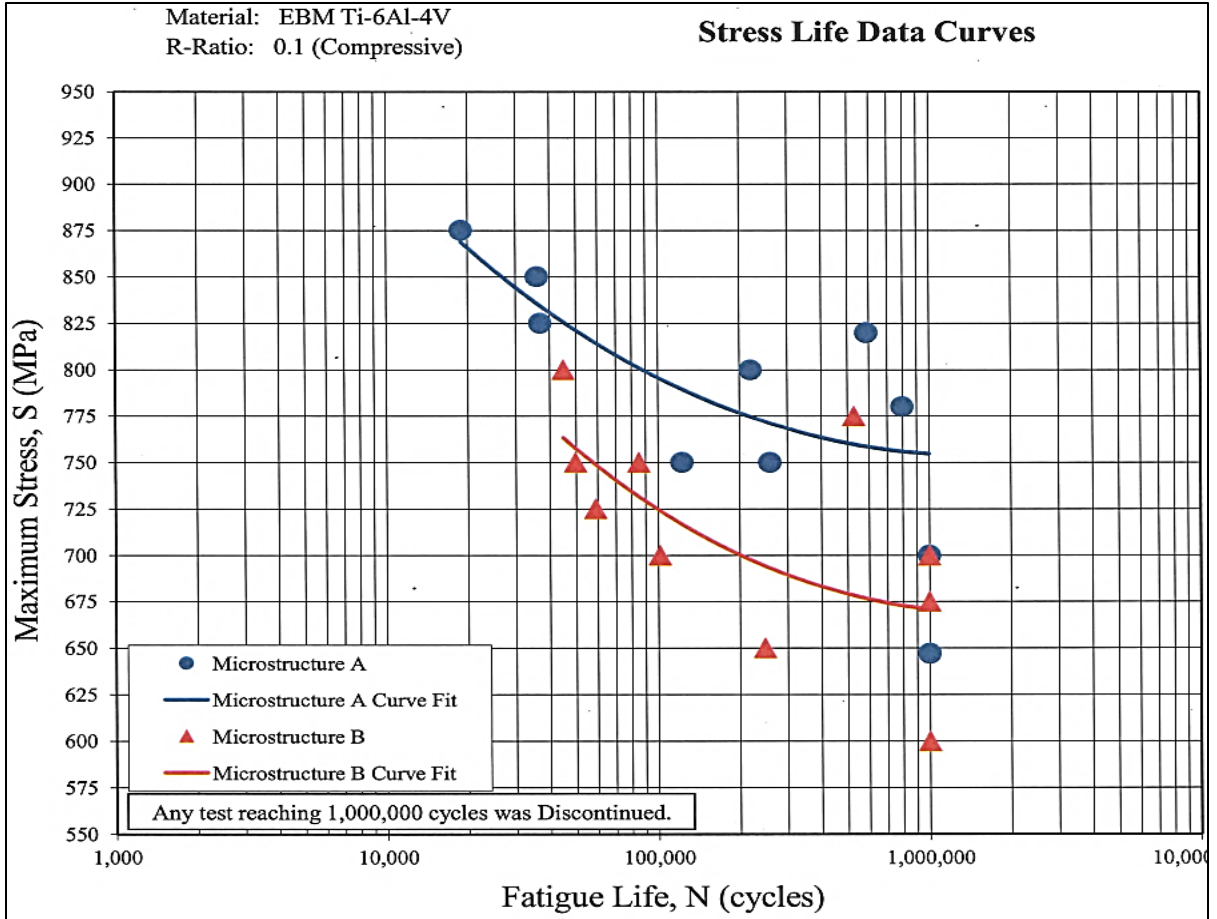
Figure 13 Stress life data for microstructure A and B reported by Westmoreland Inc.

35.5   Crack Initiation Perspective

Cyclic loading of metals undergoes plastic strain localization which leads to the formation of bands or concentrated slip. It was established that locations of bands remained visible after electro-polishing and the slip activity re-occurred at the same locations if the fatigue test continue [26]. This means they are structurally different from surrounding material and that is why they are called persistent [27]. There are three basic types of crack initiation, initiation at fatigue slip bands, initiation at grain and twin boundaries and initiation at inclusions, pores and other inhomogeneities. Initiation at fatigue slip bands is a localization of cyclic slip that results in a development of a surface with a hill-and-valley topography [26, 28]. Initiation at grain and twin boundaries is the interaction of large-angle grain boundaries at sites where the slip bands (intrusions) impinge on them. Finally inclusions, pores and other inhomogeneities can also interact with the intrusions of the well-developed slip bands (PSBs) to initiate a crack. Figure 14 shows a schematic representation of the different stages of surface relief evolution to form persistent slip bands (PSBs). One example of crack initiation is presented in figure 15 of specimen B-2 (tested at 700 Mpa). Those secondary images show the intrusion, crack propagation and different size of slip bands near to the crack.

Center Proprietary – Terms of CANFSA Membership Agreement Apply

(a) N/N$_f$ ≈ 0.04%

(b) N/N$_f$ ≈ 0.4–2.2%

M   PSB   Matrix   PSB   M

(c) N/N$_f$ ≳ 0.4–2.2%

(d) N/N$_f$ ~ 15%

0.5 µm

M   PSB   Matrix   PSB   M

M   PSB   Matrix   PSB   M

PSB embryo
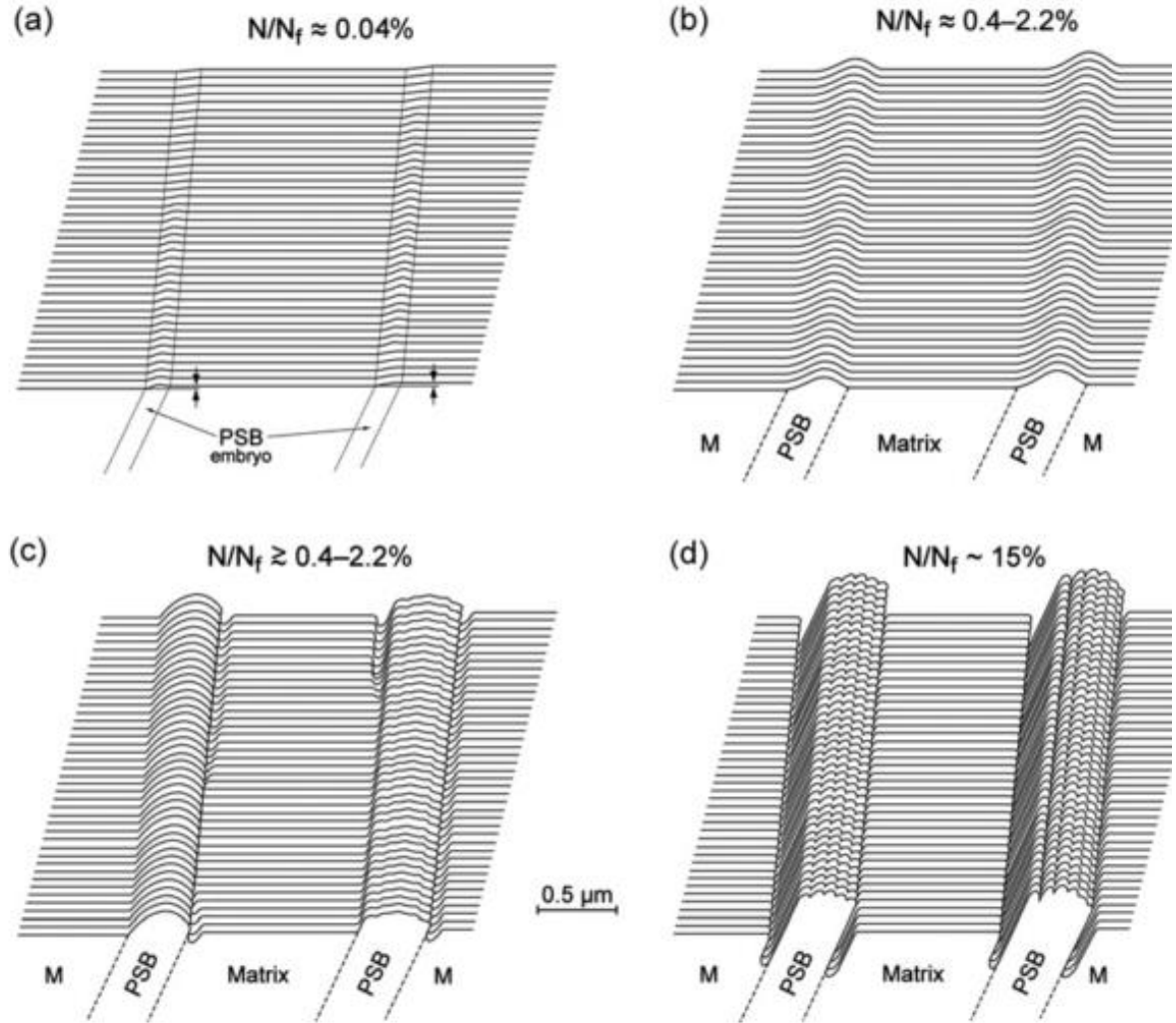
Figure 14 Stages of surface relief evolution to form (b) ribbon-like extrusions and (d) mature PSBs with well-developed intrusions at both PSB-matrix interfaces.

Different size of slip bands near to the crack

Surface deformation damage from loading roller

Surface intrusion and crack initiation site

200 µm

15 µm
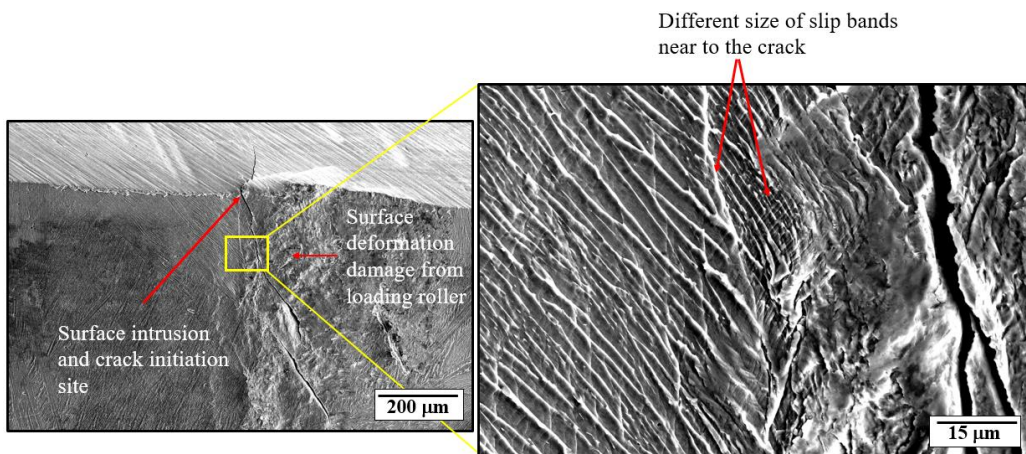
Figure 15 secondary electron micrographs of one side of specimen B-2 showing a crack initiation site.

35. 11

35.6 Comparing Microstructure A with B Under Similar Conditions

In order to compare the microstructures A and B, it is necessary to select specimens under similar conditions of stress amplitude. B-9 and A-18 were tested at 800 MPa, but B-9 failed at 44,884 cycles and A-18 failed at 220,108 cycles. Slip band length quantification was performed using the software MIPAR. Figure 16 shows one example of the process on MIPAR to measure the slip length on one specific region on samples B-9 and A-18. A manual elimination of some features was necessary to calculate the slip length on different images because they did not correspond to slip bands but were similar to them in image processing. Figure 6.6 shows the comparison between B-9 (5487 μm) and A-18 (6468 μm) of slip length and A-18 is about 15% greater than B-9. However, the stage of formation of the slip bands as explained in figure 17 is well advance for B-9 compared with A-18. The different orientation and size of slip bands on figure 15 and the different degree of slip formation (i.e. surface relief evolution) of B-9 compared with A-18 in figure 17, suggest that there is a preferential α colony orientation respect to the loading direction for the slip band formation. A closer backscatter image in figure 18 shows that difference in stage of slip band formation for both specimens.
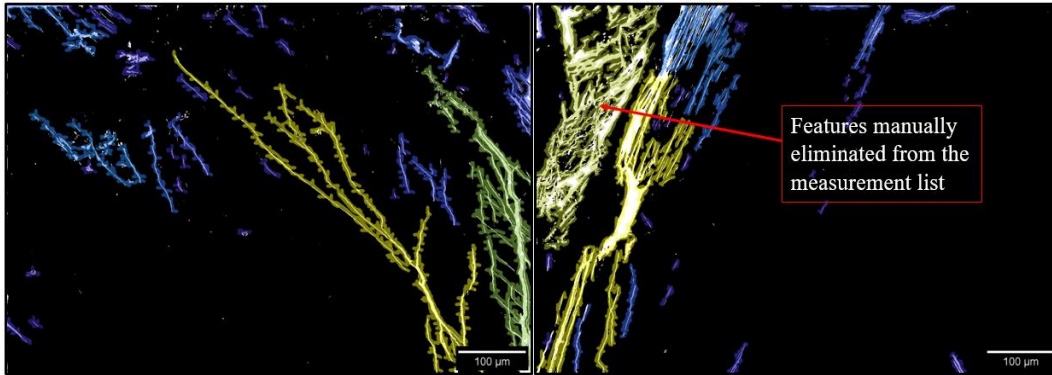
Figure 16 One example of the slip length measurement on MIPAR.
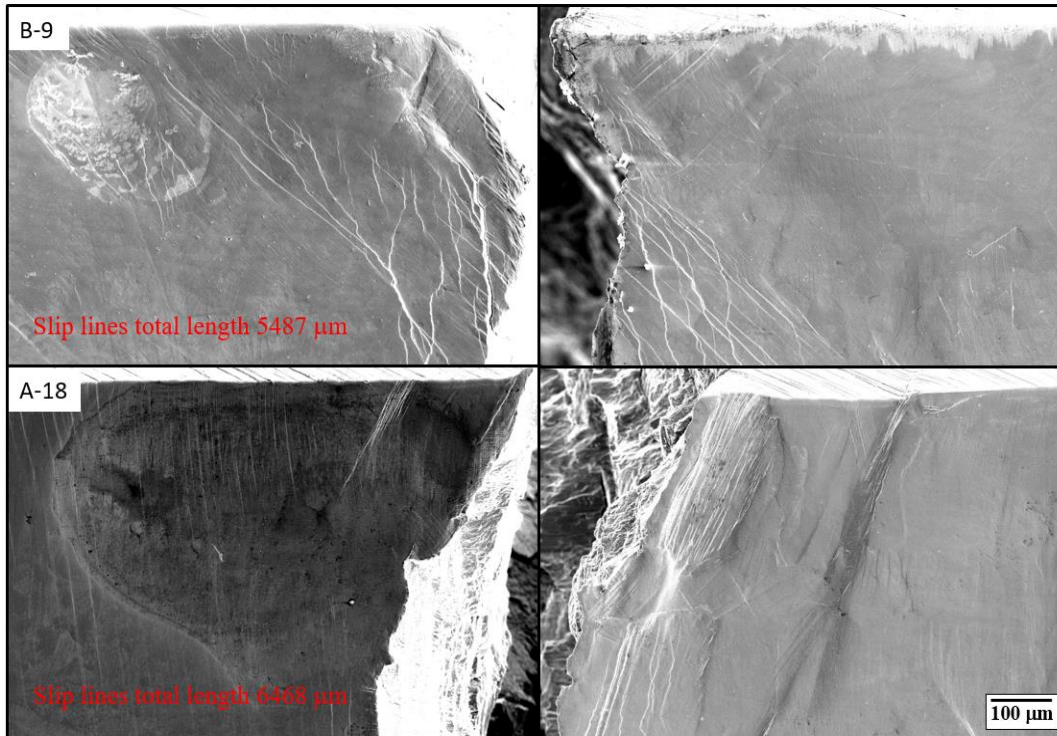
Figure 17 Secondary-electron images to compare B-9 and A-18.

35. 12
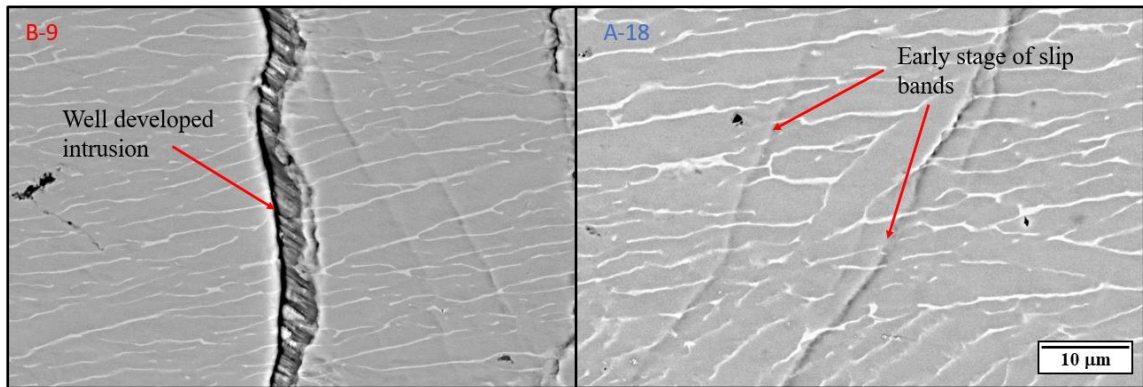
Figure 18 Backscatter images of B-9 and A-18 showing the different stage of slip band formation.

More observation on specimen A-18 at the etched surface, reveals more visible slip bands. Near to the fracture surface some α colonies were presenting visible slip bands formation, but some others do not. Figure 19a shows one α colony with the laths oriented perpendicular to the fracture surface with a high concentration of slip bands. On the other side, adjacent α colonies do not show visible slip band formation. A closer view in figure 19b reveals the existence of dark and small early stage slip bands on the α colony next to the one highly populated with shiny slip bands. Figure 19b also shows small white features inside the α laths.
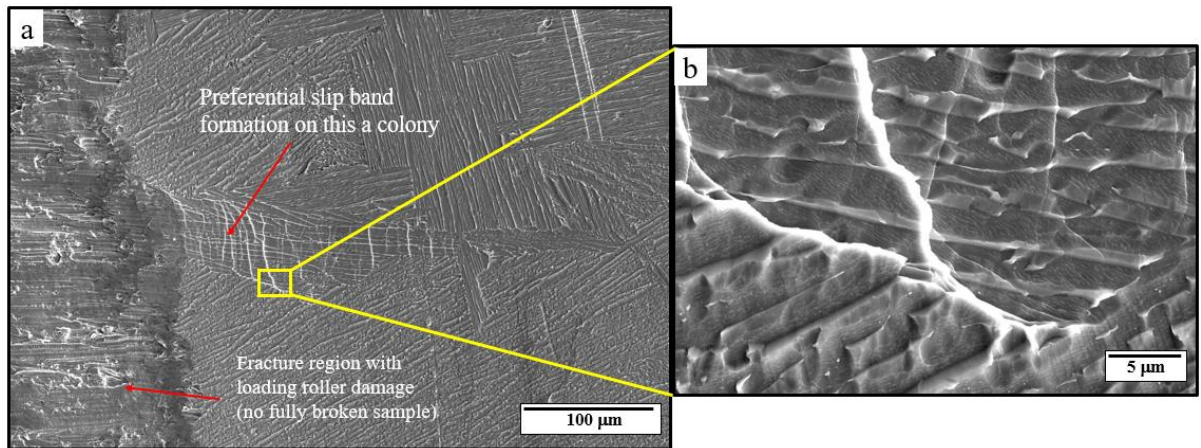
Figure 19 Secondary images of A-18 (etched side).

35.7   Crack Propagation Perspective

These EBAM-Ti-6Al-4V specimens have fully lamellar microstructure where slip or crack propagation barriers are α/β interface < α colony boundaries < prior-beta grain boundaries in that order of strength. α/β interface can transfer the slip by the parallel slip system (110) $[1\bar{1}1]_\beta$ II (0002) $[11\bar{2}0]_\alpha$ or others that are off by only 10º. Figure 20a shows an example of α/β interface acting as a barrier in specimen A-1. α Colony boundaries in figure 20b are boundaries of different orientation clusters of α laths that represent a stronger obstacle for slip or crack propagation compared with α/β interface. Prior-beta grain boundary in figure 20c is the strongest barrier for slip or crack propagation due to the presence of continuous α layers and the orientation transition to a completely different oriented β grain with different internal variants of α colonies.

35. 13
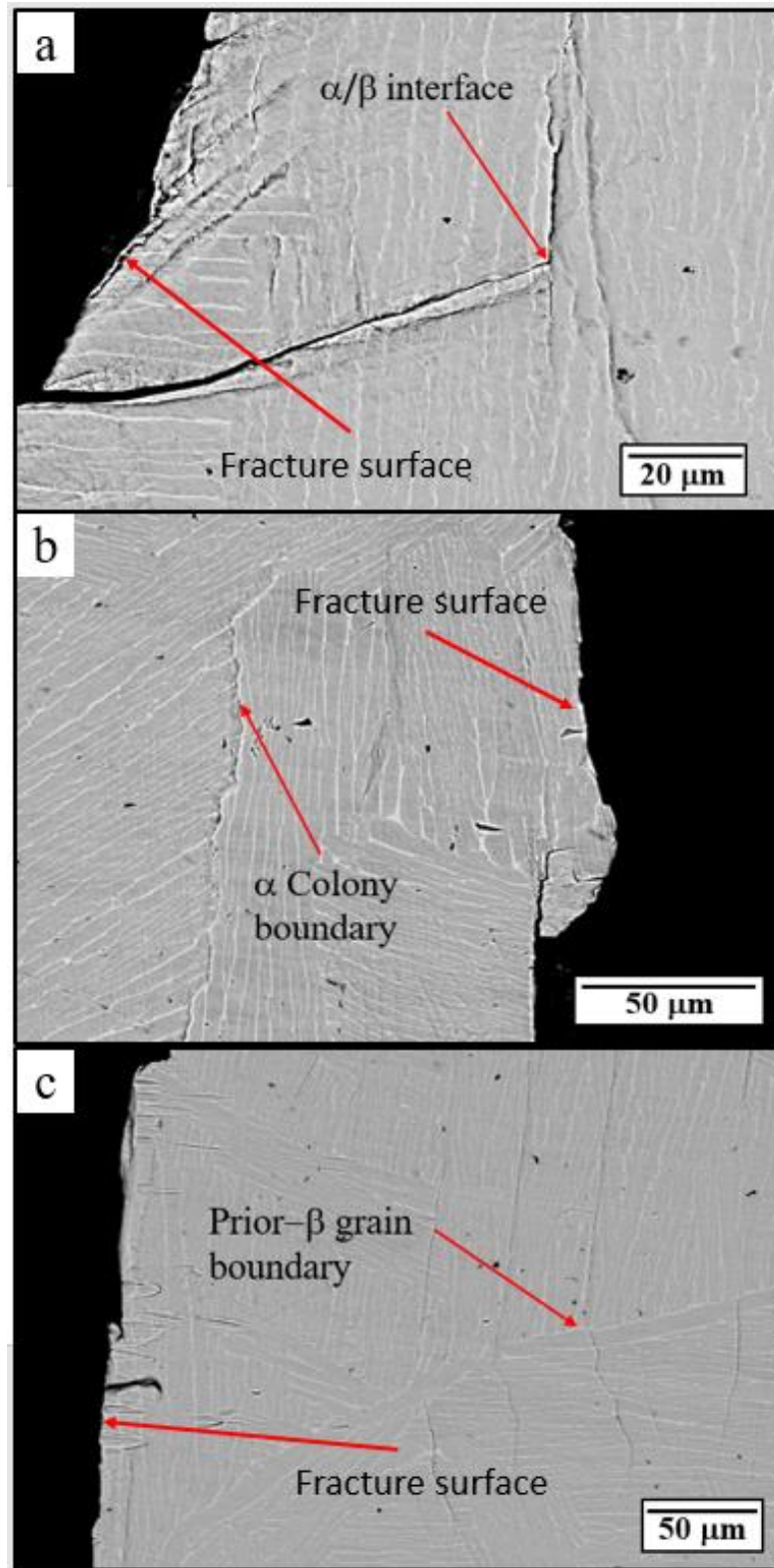
Figure 20 Examples of slip or crack propagation barriers on fatigue specimens (a) A-1 (b) B-2 and (c) B-9.

35. 14
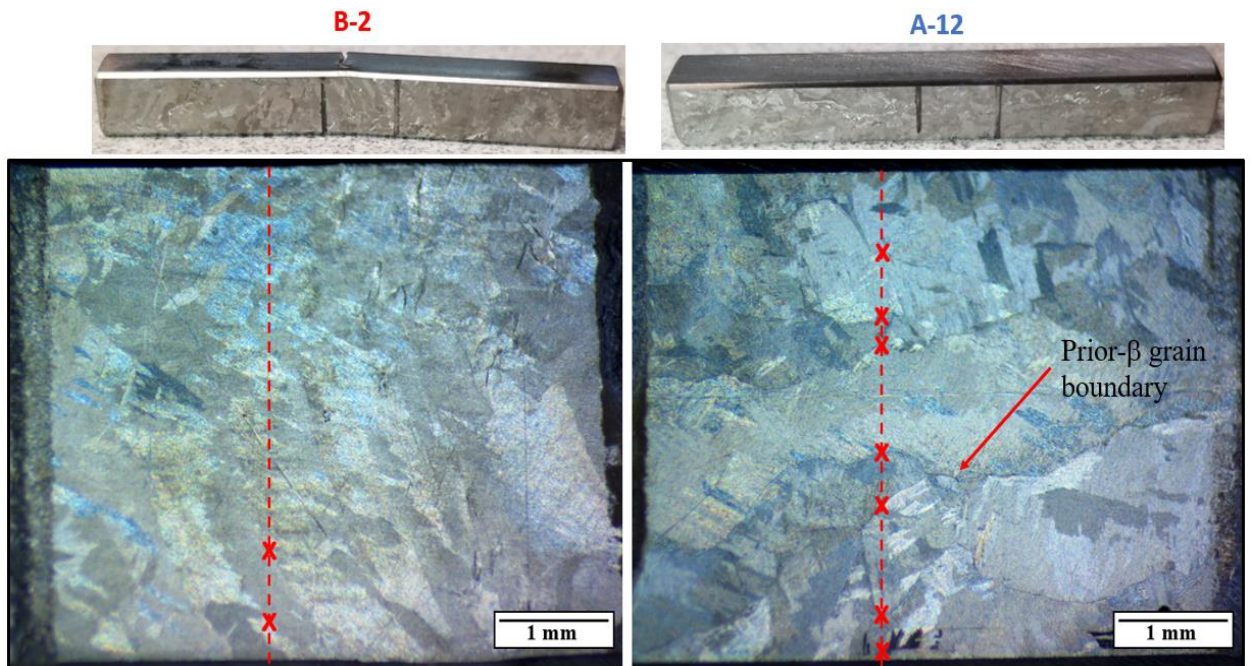
Figure 21 Optical images of bending specimens comparing B-2 with A-12
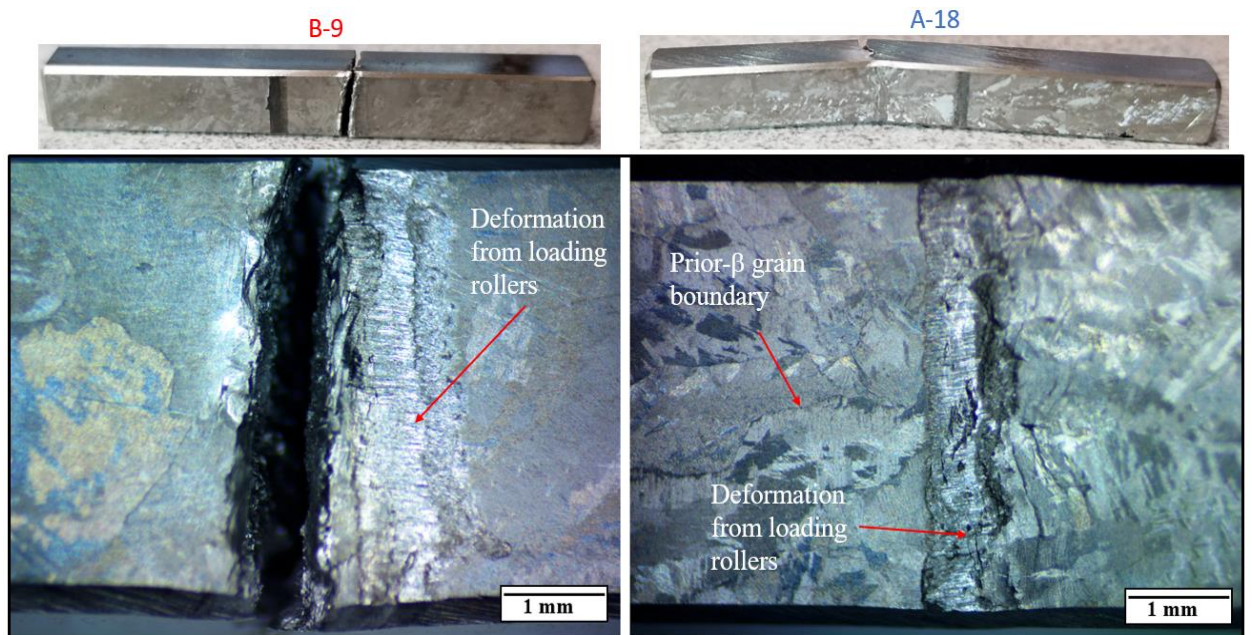
Figure 22 Optical images of bending specimens comparing B-9 with A-18

35. 15

35.8 Comparing Microstructure A with B Under Similar Conditions

In order to compare the microstructure A with B under the crack propagation perspective, it is necessary to select specimens under same conditions of stress amplitude. B-2 and A-12 were tested at a maximum stress of 700 MPa, but B-2 failed at 101,753 cycles and A-12 reached the limit of 1,000,000 cycles (runout). Optical images of the specimen A-12 revealed the presence of prior-beta grain boundaries oriented perpendicular to the fracture direction as a consequence of the bending fatigue test. In addition to this unfavorable orientation for crack propagation of those grain boundaries in A-12, they are statistically more present in specimen A-12 compared with B-2. Figure 21 shows those optical images and comparison. Additionally, optical images in figure 22 comparing B-9 with A-18 also show the same trend as described for the previous set of samples for crack propagation.

In conclusion, the stress life data indicates in general terms the better fatigue performance of microstructure A compared with B. Optical and electron microscope analysis suggests two perspectives to explain such behavior. From crack initiation perspective, the slip band formation is in a more advance stage in microstructure B compared with A due to the more random α colony orientation that provides a better opportunity to hcp slip systems being aligned with the loading direction in the bending test. From crack propagation perspective, the orientation of the columnar grains provide a statistically more presence of prior-beta grain boundaries perpendicular to the slip band lines or crack propagation. These two factors may explain the better performance of microstructure A.

Excluding those 5 specimens (3 of microstructure B and 2 of microstructure A) who never failed (runout) from the stress life data curves (see fig.13), we can observe that all red triangles (B microstructure) failed at lower maximum stress than blue circles (A microstructure) except B-9 (800 MPa) and B-8 (775 MPa). However, the A specimens with the same maximum stress of those two B exceptions such as A-18 (800 MPa) and A-14 (780 MPa) failed at a much higher number of cycles than their similar of microstructure B. Another important observation is that above 700 MPa there is not a single runout specimen. The two specimens of microstructure B that failed below 700 MPa (B-2 and B3) may contain random microcracks or defects that are inherent to the manufacturing process.

35.9 References

[1] P. Wanjara, M. Jahazi, Linear friction welding of Ti-6Al-4V: Processing, microstructure, and mechanical-property inter-relationships, Metallurgical and Materials Transactions A 36(8) (2005) 2149-2164.

[2] J. Romero, M.M. Attallah, M. Preuss, M. Karadge, S.E. Bray, Effect of the forging pressure on the microstructure and residual stress development in Ti–6Al–4V linear friction welds, Acta Materialia 57(18) (2009) 5582-5592.

[3] I. Bhamji, M. Preuss, P.L. Threadgill, A.C. Addison, Solid state joining of metals by linear friction welding: a literature review, Materials Science and Technology 27(1) (2011) 2-12.

[4] M. Karadge, M. Preuss, C. Lovell, P.J. Withers, S. Bray, Texture development in Ti–6Al–4V linear friction welds, Materials Science and Engineering: A 459(1-2) (2007) 182-191.

[5] Y. Guo, Y. Chiu, M.M. Attallah, H. Li, S. Bray, P. Bowen, Characterization of dissimilar linear friction welds of α-β titanium alloys, Journal of materials engineering and performance 21(5) (2012) 770-776.

[6] A.R. McAndrew, P.A. Colegrove, C. Bühr, B.C.D. Flipo, A. Vairis, A literature review of Ti-6Al-4V linear friction welding, Progress in Materials Science 92 (2018) 225-257.

[7] A. Vairis, M. Frost, High frequency linear friction welding of a titanium alloy, Wear 217(1) (1998) 117-131.

[8] A. Vairis, M. Frost, On the extrusion stage of linear friction welding of Ti 6Al 4V, Materials Science and Engineering: A 271(1-2) (1999) 477-484.

[9] A.R. McAndrew, P.A. Colegrove, A.C. Addison, B.C.D. Flipo, M.J. Russell, Energy and Force Analysis of Ti-6Al-4V Linear Friction Welds for Computational Modeling Input and Validation Data, Metallurgical and Materials Transactions A 45(13) (2014) 6118-6128.

[10] W.Y. Li, T. Ma, Y. Zhang, Q. Xu, J. Li, S. Yang, H. Liao, Microstructure Characterization and Mechanical Properties of Linear Friction Welded Ti-6Al-4V Alloy, Advanced Engineering Materials 10(1-2) (2008) 89-92.

[11] W. Li, H. Wu, T. Ma, C. Yang, Z. Chen, Influence of Parent Metal Microstructure and Post-Weld Heat Treatment on Microstructure and Mechanical Properties of Linear Friction Welded Ti-6Al-4V Joint, Advanced Engineering Materials 14(5) (2012) 312-318.

[12] K. Hiroshi, N. Koji, T. Wakabayashi, N. Kenji, Application of linear friction welding technique to aircraft engine parts, IHI Engineering Review 47(1) (2014) 40-43.

[13] P.C. Collins, D.A. Brice, P. Samimi, I. Ghamarian, H.L. Fraser, Microstructural Control of Additively Manufactured Metallic Materials, Annu. Rev. Mater. Res. 46(1) (2016) 63-91.

[14] Sciaky, Sciaky's Electron Beam Additive Manufacturing (EBAM®) Process. <http://www.sciaky.com/additive-

manufacturing/wire-am-vs-powder-am>, 2019).

[15] B.J. Hayes, B.W. Martin, B. Welk, S.J. Kuhr, T.K. Ales, D.A. Brice, I. Ghamarian, A.H. Baker, C.V. Haden, D.G. Harlow, H.L. Fraser, P.C. Collins, Predicting tensile properties of Ti-6Al-4V produced via directed energy deposition, Acta Materialia 133 (2017) 120-133.

[16] T. Zhai, Y. Xu, J. Martin, A. Wilkinson, G. Briggs, A self-aligning four-point bend testing rig and sample geometry effect in four-point bend fatigue, International Journal of Fatigue 21(9) (1999) 889-894.

[17] M. Janeček, F. Nový, P. Harcuba, J. Stráský, L. Trško, M. Mhaede, L. Wagner, The Very High Cycle Fatigue Behaviour of Ti-6Al-4V Alloy, Acta Physica Polonica, A. 128(4) (2015).

[18] R. Morrissey, P.J. Golden, Ultrasonic fatigue testing of Ti-6Al-4V, Journal of ASTM International 2(5) (2005) 1-10.

[19] A. Puškár, Ultrasonic fatigue testing equipment and new procedures for complex material evaluation, Ultrasonics 31(1) (1993) 61-67.

[20] A. Puskar, The use of high-intensity ultrasonics, Amsterdam, Elsevier Scientific Publishing Co.(Materials Science Monographs. Volume 13), 1982. 302 p. Translation, 1982.

[21] J. Gong, A. Wilkinson, Ultra small scale high cycle fatigue testing by micro-cantilevers, Nanomechanical Testing in Materials Research and Development V, Grande Real Santa Eulalia Hotel, Albufeira, Portugal, 2015.

[22] M. Freitas, V. Anes, D. Montalvao, L. Reis, A. Ribeiro, Design and assembly of an ultrasonic fatigue testing machine, Anales de Mecânica de la Fractura (2011).

[23] A. Shyam, C. Torbet, S. Jha, J. Larsen, M. Caton, C. Szczepanski, T. Pollock, J. Jones, Development of ultrasonic fatigue for rapid, high temperature fatigue studies in turbine engine materials, 10th International Symposium on Superalloys, Champion, PA, September, 2004, pp. 19-23.

[24] D.M. Dimitrov, V. Mihailov, B. Kostov, Modeling of Ultrasonic Fatigue-Life Testing Machine, Proceedings of COMSOL conference, Milan, 2012.

[25] I. Ghamarian, Application of ASTAR/precession electron diffraction technique to quantitatively study defects in nanocrystalline metallic materials, (2017).

[26] J. Man, P. Klapetek, O. Man, A. Weidner†, K. Obrtlík, J. Polák, Extrusions and intrusions in fatigued metals. Part 2. AFM and EBSD study of the early growth of extrusions and intrusions in 316L steel fatigued at room temperature, Philosophical Magazine 89(16) (2009) 1337-1372.

[27] J. Man, K. Obrtlík, J. Polák, Extrusions and intrusions in fatigued metals. Part 1. State of the art and history†, Philosophical Magazine 89(16) (2009) 1295-1336.

[28] P. Lukáš, L. Kunz ‡, Role of persistent slip bands in fatigue, Philosophical Magazine 84(3-5) (2004) 317-330.